



HAL
open science

Supercritical transition to turbulence in an inertially-driven von Karman closed flow

Florent Ravelet, Arnaud Chiffaudel, François Daviaud

► **To cite this version:**

Florent Ravelet, Arnaud Chiffaudel, François Daviaud. Supercritical transition to turbulence in an inertially-driven von Karman closed flow. 2006. hal-00118719v1

HAL Id: hal-00118719

<https://hal.science/hal-00118719v1>

Preprint submitted on 14 Dec 2006 (v1), last revised 22 Jan 2008 (v3)

HAL is a multi-disciplinary open access archive for the deposit and dissemination of scientific research documents, whether they are published or not. The documents may come from teaching and research institutions in France or abroad, or from public or private research centers.

L'archive ouverte pluridisciplinaire **HAL**, est destinée au dépôt et à la diffusion de documents scientifiques de niveau recherche, publiés ou non, émanant des établissements d'enseignement et de recherche français ou étrangers, des laboratoires publics ou privés.

Supercritical transition to turbulence in an inertially-driven von Kármán closed flow.

By FLORENT RAVELET ¹†, ARNAUD CHIFFAUDEL¹
AND FRANCOIS DAVIAUD¹

¹Service de Physique de l'Etat Condensé, Direction des Sciences de la Matière, CEA-Saclay,
CNRS URA 2464, 91191 Gif-sur-Yvette cedex, France

(Received (not yet): 5 December 2006)

We study the transition from basic state to fully developed turbulence for an inertially-driven von Kármán flow between two counter-rotating large impellers fitted with curved blades. The laminar basic flow is very similar to the flow between smooth disks in an effective aspect ratio. The transition to turbulence in this closed flow is globally supercritical and is driven by the destabilisation of the azimuthal shear-layer, *i.e.*, Kelvin–Helmholtz instability. Quasi-periodicity and chaos precedes the emergence of turbulent spectra. The energy of the velocity fluctuations can be used as an order parameter to characterize the transition. This quantity defines a critical Reynolds number Re_c for the appearance of time-dependence in the flow, and an upper threshold Re_t for the saturation of the instability cascade which can be viewed as a threshold for developed turbulence. The turbulent dissipation measured as a dimensionless drag coefficient reaches a plateau past this finite value Re_t , as expected for a “Kolmogorov” turbulence for $Re \rightarrow \infty$. The spectral analysis in temporal domain reveals that almost all of the fluctuations energy is stored in time-scales one or two orders of magnitude slower than the time-scale based on impeller frequency. The transformation of the time-spectrum from a peak-frequency spectrum to a continuous spectrum is described and discussed.

1. Introduction

Hydrodynamic turbulence is rather a general rule than an exception in fluid flows. For instance it is a key feature for weather forecast, contaminants dispersion, sediments transport or engineering problems such as drag increase due to the turbulent wake of cars (see the reference books of Tennekes & Lumley 1972; Lesieur 1990). In a few ideal cases, exact solutions of the Navier–Stokes equations are available, based on several assumptions such as auto-similarity, stationarity, or symmetry (for a collection of examples, see Schlichting 1979). Unfortunately, they are often irrelevant in practice, because they are unstable. Two of the simplest examples are the centrifugal instability of the Taylor–Couette flow between two concentric cylinders, and the onset of Rayleigh–Bénard convection between two differentially heated plates: once the amount of angular momentum or heat is too important to be carried by molecular diffusion, a more efficient convective transport arises. Increasing further the parameter control in these two examples, secondary bifurcations occur, leading rapidly to temporal chaos, and/or to spatio-temporal chaos, then to turbulence. A universal understanding of the transition to turbulence is far from available and

† Present address: Laboratory for Aero and Hydrodynamics, Leeghwaterstraat 21, 2628 CA Delft, The Netherlands

several scenarii, such as the Landau, the Ruelle–Takens or the Spatio-Temporal Intermittency scenarii have been widely discussed in the last decades (see for instance Berge *et al.* 1984; Manneville 1990; Cross & Hohenberg 1993). Differences in the transition process have been found depending on the system class (small *vs.* extended systems). Furthermore, the transition can even be globally subcritical in some open shear flows (see for instance Dauchot & Manneville 1997; Grossmann 2000).

1.1. *Instabilities of the von Kármán swirling flow between flat disks*

The disk flow is an example where exact Navier–Stokes solutions are available. The original problem of the flow of a viscous fluid over an infinite rotating flat disk has been considered by von Kármán (1921) who was looking for self-similar exact solutions of the stationary axisymmetric Navier–Stokes equations (this work is well described in Schlichting 1979). Experimentally, the problem of an infinite disk in an infinite medium is difficult to address. Addition of a second coaxial disk has been proposed by Batchelor (1951) and Stewartson (1953). A cylindrical housing to the flow can also be added. Instabilities and transitions have been extensively studied in this system (for instance in Mellor *et al.* 1968; Harriott & Brown 1984; Escudier 1984; Sørensen & Christensen 1995; Gelfgat *et al.* 1996; Spohn *et al.* 1998; Gauthier *et al.* 1999; Schouveiler *et al.* 2001; Nore *et al.* 2003, 2004, 2005). The basic principle of this flow is the following: a layer of fluid is carried near the disk by viscous friction and is thrown outwards by centrifugation. By incompressibility of the flow, fluid is pumped toward the centre of the disk. The first numerical studies of this problem have been carried out by Cochran (1934). Since the review of Zandbergen & Dijkstra (1987), this family of flow is called “von Kármán swirling flow”. In all cases, it deals with the flow between smooth disks, at low-Reynolds numbers, enclosed or not into a cylindrical container. We will focus on the results of Nore *et al.* (2003, 2004, 2005), who study the exact counter-rotating regime where the flow is divided into two toric cells separated by an azimuthal shear-layer, *i.e.* the situation described in the present article. The Reynolds-number range covered in their studies is $140 \leq Re \leq 600$, with flat disks.

1.2. *The “French washing machine”: an inertially-driven, highly turbulent von Kármán swirling flow.*

In the meanwhile, several approaches have been carried in parallel concerning developed turbulence, focused on statistical properties of flow quantities at small scales (Frisch 1995) or taking into account the persistence of coherent structures in a more deterministic point of view (Tennekes & Lumley 1972; Lesieur 1990). One of the major difficulty concerning a self-consistent statistical treatment of turbulence is that turbulence itself is not an intrinsic property of the fluid, but strongly depends on the flow in which it takes place. Nevertheless, some universal statistics are expected in the limit of infinite Reynolds numbers ($Re \rightarrow \infty$) (see Frisch 1995). Experimentally, the so-called “French washing-machine” has been a basis for extensive studies of very high-Reynolds number turbulence in the last decade (Douady *et al.* 1991; Fauve *et al.* 1993; Zocchi *et al.* 1994; Cadot *et al.* 1995; Labbé *et al.* 1996; Tabeling *et al.* 1996; Cadot *et al.* 1997; La Porta *et al.* 2001; Moisy *et al.* 2001; Titon & Cadot 2003; Leprovost *et al.* 2004; Marié & Daviaud 2004; Ravelet *et al.* 2004). To reach a Kolmogorov regime in these studies, a von Kármán flow is inertially-driven between two disks fitted with blades, at a very high-Reynolds number ($10^5 \lesssim Re \lesssim 10^7$). Due to the inertial stirring, very high turbulence levels can be reached, with fluctuations up to 50% of the blades velocity, as we shall see in this article. It first allowed extensive studies of intermittency at small scales of turbulence (Zocchi *et al.* 1994; Tabeling *et al.* 1996; Moisy *et al.* 2001). This flow is also a prototype

for strongly non homogeneous non isotropic turbulence (Zocchi *et al.* 1994), and without any neat mean flow, the Taylor hypothesis is no longer suitable (Pinton & Labbé 1994). In addition, La Porta *et al.* (2001) carried out one of the first Lagrangian studies in this type of flow. Labbé *et al.* (1996); Titon & Cadot (2003); Leprovost *et al.* (2004) also studied the statistics of global quantities such as the injected power statistics. The role of large scales structures on turbulent momentum transfer has been highlighted by Marié & Daviaud (2004).

In any particular turbulent flow, the statistical properties at a finite Re could still depend on the way the flow became turbulent. Several people measured or reported very long time fluctuations in the turbulent von Kármán flow, leading to spectra behaving as f^{-1} at frequencies two order of magnitude lower than the injection frequency (Zocchi *et al.* 1994; Bourgoin *et al.* 2002; Ravelet 2005). The construction of the spectrum with Re is studied in the present paper.

Moreover, we have shown that the large scale structure of the flow could be unstable in some cases, a phenomenon we called “global” or “turbulent bifurcation” for it seems to happen only for a turbulent flow (Ravelet *et al.* 2004). In this last work, we discussed about the respective role of the turbulent fluctuations and of the changes in the mean-flow structure with increasing the Reynolds number. The purpose of the present article is thus to characterize the transition to turbulence in an inertially-driven von Kármán flow. We give in the next paragraph a short definition of turbulence, and a review of the different tools to characterize the transition to turbulence.

1.3. *Experimental characterization of the transition to turbulence in a closed flow*

At very low-Reynolds number a flow is usually laminar, *i.e.* spatially smooth and stationary or periodic in time. Visualisations of the basic laminar state are thus a good tool to characterize the flow and will help us to understand the first steps in the transition to turbulence. Although a clear definition of turbulence is hard to give, a flow is called turbulent when it presents the following features (Lesieur 1990):

- (a) it is unpredictable at long times;
- (b) the transport and mixing properties are enhanced with respect to molecular diffusion processes;
- (c) the velocity field is rough and has a wide range of spatial and temporal scales.

The two first properties are shared with chaotic flows. We will thus have to deal with dynamical system tools. With the use of these, great advances have been made in the understanding of transition to turbulence these two last decades, following the cascade of bifurcations which lead to turbulence in different types of systems. In our case, we should expect a globally supercritical transition, due to a Kelvin–Helmholtz instability (Nore *et al.* 2004). Here again, we will use flow visualisations to follow the very first bifurcations. We will then try and identify some flow quantities as order parameters for a quantitative measurement of the bifurcation characteristics.

The last property (c) deals with statistical tools, the spatial power spectrum of velocity fluctuations being expected to behave as a $k^{-5/3}$ power-law in the limit of vanishing viscosity or infinite Re as stated by Kolmogorov (1991*a,b*), (see for instance Frisch 1995; Lesieur 1990). This kind of experimental measurements are usually performed in the time domain, and extrapolated to the space domain. This kind of analysis is suitable for jet or grid turbulence, with the help of the Taylor Hypothesis. We will see in this article that in our closed shear-flow the temporal power spectra of fluctuations measured in the shear-layer are very close to behave as a power law at high frequencies, and exhibit interesting behaviours at very low frequencies, down to one hundredth of the impeller rotation frequency.

In a more global point of view, the study of the scaling of energy dissipation with the Reynolds number is a common tool which characterizes the flow regime. For instance, in a pipe flow, the dimensionless pressure drop scales like $64Re^{-1}$ in the laminar regime (Schlichting 1979). The dimensionless torque exerted on a housed disk should also scale like Re^{-1} in a laminar flow. For open flow on a flat plate, (resp. for a disk in an infinite medium) the friction coefficient (the dimensionless torque) scales like $Re^{-1/2}$, due to the formation of a laminar boundary layer (Schlichting 1979). But, when turbulence arises, the observed scaling for these quantities is different. In free shear-flows or in open bounded-flows, turbulence models such as the mixing-length or wall laws are suitable under several assumptions (only one imposed length scale, small fluctuations with respect to a mean flow, see Tennekes & Lumley 1972). These models predict other scalings for the dimensionless friction coefficients, with power-laws (the dimensionless torque scales like $Re^{-1/5}$ for the free disk flow with the use of Blasius 1/7th wall law) or with logarithmic corrections. In a closed wall-bounded shear-flow, more precisely a Taylor–Couette flow, the study of the scaling of the torque evidenced a transition between two different turbulent regimes (Lathrop *et al.* 1992). Moreover, in the case of rough boundaries, a final Kolmogorov-regime is usually observed, where the dimensionless friction becomes independent of Re (Schlichting 1979; Cadot *et al.* 1997; van den Berg *et al.* 2003; Gioia & Chakraborty 2006; Goldenfeld 2006). We will thus also follow the evolution of the scaling of dissipation with the Reynolds number in our experiment.

1.4. Outline of the present article

In this article, we first describe the experimental setup, the fluid properties and the measurement techniques in §2. We then characterize the basic laminar flow and its first instabilities in §3. In §4 we describe the transition from the laminar regime to turbulence through quasi-periodicity and chaos and explore the construction of the temporal spectrum of velocity fluctuations. We then summarize and discuss the main results in §5.

2. Experimental setup

2.1. Dimensions, symmetries and control parameter

The cylinder radius and height are, respectively, $R_c = 100$ mm and $H_c = 500$ mm. A sketch of the experiment can be found in figure 1(a). We use bladed disks to ensure inertial stirring. Most of the inertially-driven von Kármán setups studied in the past dealt with straight blades (Cadot *et al.* 1995; Labbé *et al.* 1996). Here, the impellers consist of 185 mm diameter stainless-steel disks each fitted with 16 curved blades, of curvature radius 50 mm and of height $h = 20$ mm (figure 1b). The distance between the inner faces of the disks is $H = 180$ mm, which defines a flow volume of aspect ratio $H/R_c = 1.8$. With the curved blades, the directions of rotation are no longer equivalent and we can either rotate the impellers anticlockwise (with the convex face of the blades forward, direction +) or clockwise (with the concave face of the blades forward, direction –).

The impellers are driven by two independent brushless 1.8 kW motors, with speed servo loop control. The maximal torque they can reach is 11.5 N.m. The motor rotation frequencies $\{f_1; f_2\}$ can be varied independently in the range $1 \leq f \leq 15$ Hz. Below 1 Hz, the speed regulation is not efficient enough, and the dimensional quantities are measured with insufficient accuracy. We will consider exact counter-rotating regimes $f_1 = f_2$ in this article and the imposed speed of the impellers will be referred as f .

The experimental setup is thus axisymmetric and symmetric towards rotations of π around any radial axis passing through the centre O (\mathcal{R}_π -symmetry), and we will consider here only \mathcal{R}_π -symmetric mean solutions, though mean flows breaking this symmetry do

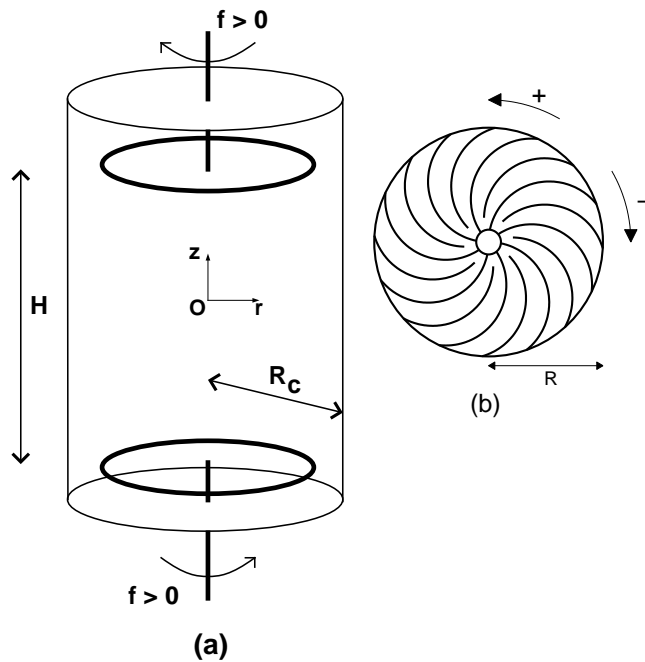


FIGURE 1. (a) Sketch of the experiment. The flow volume between the impellers is of height $H = 1.8 R_c$. (b) Impellers used in this article. The disks radius is $R = 0.925 R_c$ and they are fitted with 16 curved blades: the two different directions of rotation defined here are not equivalent. This model of impellers has been used in the VKS1 sodium experiment (Bourgoin *et al.* 2002) and is called TM60.

C	μ at 15°C	μ at 30°C	ρ	Re range
99%	1700	580	1260	50 – 2000
93%	590	210	1240	130 – 5600
85%	140	60	1220	$5.5 \times 10^2 - 1.9 \times 10^4$
81%	90	41	1210	$8.4 \times 10^2 - 2.8 \times 10^4$
74%	43	20	1190	$1.8 \times 10^3 - 5.6 \times 10^4$
0%	1.1	0.8	1000	$5.7 \times 10^4 - 1.2 \times 10^6$

TABLE 1. Dynamic viscosity μ (10^{-3} Pa.s) at various temperatures, density ρ (kg.m^{-3}) at 20°C and achievable Reynolds number range for various mass concentrations C of glycerol in water.

exist for these impellers, at least at very high-Reynolds numbers (Ravelet *et al.* 2004). The study of the Reynolds number dependence of the “global turbulent bifurcation” is out of the scope of the present article and will be presented elsewhere. Also, since we drive the impellers independently, there is always a tiny difference between f_1 and f_2 and the \mathcal{R}_π -symmetry of the system cannot be considered as exact. In the following, we will keep using this symmetry —very useful to describe the observed patterns— but we will keep in mind that our system is only an approximation of a \mathcal{R}_π -symmetric system. The consequences on the dynamics will be analyzed in the discussion (§ 5.1).

In the following, all lengths will be expressed in units of R_c . We also use cylindrical coordinates $\{r ; z\}$ and the origin is on the axis of the cylinder, and equidistant from

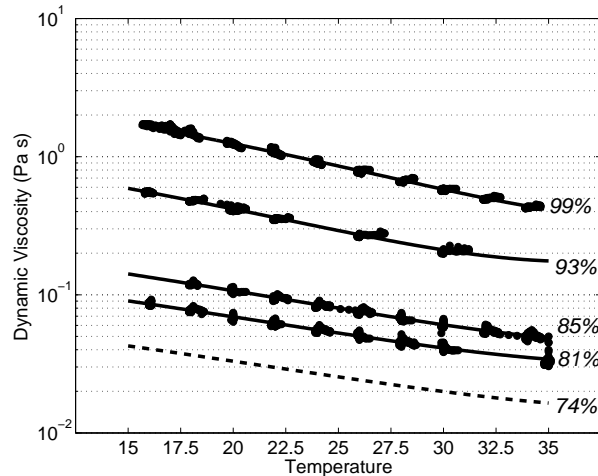


FIGURE 2. Dynamic viscosity of the various mixes *vs.* temperature in $^{\circ}\text{C}$. The mass concentration in glycerol are given in percentage. The points are measured in a Couette viscometer, and the continuous lines are second order polynomial fits. The dashed line is a fit on the data of Hodgman (1947).

the two impellers to take advantage of the \mathcal{R}_{π} -symmetry (see figure 1a). The time unit is defined with the impeller rotation frequency f . The integral Reynolds number Re is thus defined as $Re = 2\pi f R_c^2 \nu^{-1}$ with ν the kinematic viscosity of the fluid. In our previous works (Leprovost *et al.* 2004; Marié & Daviaud 2004; Ravelet *et al.* 2004, 2005), we used water at 20 – 30 $^{\circ}\text{C}$ as working fluid. The Reynolds numbers range we can reach with this fluid is thus: $6.3 \times 10^4 \lesssim Re \lesssim 1.2 \times 10^6$. To decrease Re down to laminar regimes, *i.e.* to a few tens, we need a fluid with a kinematic viscosity a thousand times greater than that of water. We thus use 99%-pure glycerol which kinematic viscosity is $0.95 \times 10^{-3} \text{ m}^2 \cdot \text{s}^{-1}$ at 20 $^{\circ}\text{C}$ (Hodgman 1947) and should be able to study the range $50 \lesssim Re \lesssim 900$. To cover a wide range of Reynolds numbers and match these two extreme ranges, we then use different mixes of glycerol and water, at temperatures between 15 and 35 $^{\circ}\text{C}$. The physical properties of these mixtures are given in table 1, where C is the mass percentage of glycerol in the mixture. The viscosities of samples of the solutions are measured in a Couette viscosimeter (figure 2). We varied the shear rate in the range 100 – 1500 s^{-1} . For a pure fluid an Arrhenius law usually describes the temperature dependence of the dynamic viscosity; nevertheless the law for a mix of fluids is not that simple (Nguyen *et al.* 2004). We thus fit the temperature dependence by a second order polynomial law (figure 2). To compute the kinematic viscosity, we finally use these fits and the density at 20 $^{\circ}\text{C}$ (table 1), neglecting the temperature dependence of the density.

We use several fluids of different viscosities in order to cover a wide range of Reynolds numbers. Moreover, the viscosity of the fluids is approximately five times greater at 15 $^{\circ}\text{C}$ than at 35 $^{\circ}\text{C}$ as can be seen in figure 2. We thus need to control the temperature and installed rolled copper tubes behind the impellers, in which water coming from a thermal bath circulates. Plexiglas disks can be mounted between the impellers and the copper tubes to hydrodynamically isolate the von Kármán flow volume and thus reduce the turbulent coupling between the back side of the impellers and the heat exchanger. They are at typically 50 mm of the impeller back side. However, these disks reduce the thermal coupling: they are used in turbulent water flows and taken away in low-Reynolds-number flows. The temperature of the working fluid is measured with a platinum thermoresistance

(Pt100) mounted on the cylinder wall ($\{r = 1 ; z = 0\}$). An expansion bucket is also hold on the roof of the experimental room in order to get rid of bubbles.

2.2. Experimental tools, dimensionless measured quantities and experimental errors

Several techniques have been used in parallel: flow visualisations with light sheets and air bubbles, torque measurements and velocity measurements.

Flow visualisations are made in vertical planes illuminated by approximately 2 mm thick light sheets. We look at two different positions with respect to the flow: either the central meridian plane where the visualised components are the radial and axial ones or in a plane almost tangent to the cylinder wall where the azimuthal component dominates. Tiny air bubbles (less than 1 mm) are used as tracing particles.

Torques are measured as an image of the current consumption in the motors given by the servo drives and have been calibrated by calorimetry. Brushless motors are known to generate electromagnetic noise, due to the Pulse-Width-Modulation supply. We use armored cables and triphase sinusoidal output filters (Schaffner FN5010-8-99), and the motors are enclosed in Faraday cages, which enhances the quality of the measurements. The minimal torques we measured are above 0.3 N.m, and we estimate the error in the measurements to be ± 0.1 N.m. The torques T will be presented in the dimensionless form:

$$K_p = T (\rho R_c^5 (2\pi f)^2)^{-1}$$

Velocity fields are measured by Laser Doppler Velocimetry (LDV). We use a single component DANTEC device, with a He-Ne Flowlite Laser (wave length 632.8 nm) and a BSA57N20 Enhanced Burst Spectrum Analyzer. The geometry of the experiment allows us to measure in one point either the axial component $V_z(t)$ or the azimuthal component $V_\theta(t)$. Though the time-averaged velocity field \mathbf{V} is not a solution of the Navier-Stokes equations, it is a solenoidal vector field, and it is axisymmetric. We thus use the incompressibility condition $\nabla \cdot \mathbf{V} = 0$ to compute the remaining radial component V_r . In cylindrical coordinates and for an axisymmetric velocity field it writes:

$$\frac{1}{r} \frac{\partial r V_r}{\partial r} + \frac{\partial V_z}{\partial z} = 0$$

$$V_r(r, z) = -\frac{1}{r} \int_0^r r' \frac{\partial V_z}{\partial z}(r', z) dr'$$

We also define the poloidal stream function:

$$\Psi(r, z) = \frac{1}{r} \int_0^r r' V_z(r', z) dr'$$

In the following, all the velocities will be presented in a dimensionless form:

$$\mathbf{v} = (2\pi R_c f)^{-1} \mathbf{V}$$

The measurements of the time-averaged velocity field are performed on a $\{r \times z\} = 11 \times 17$ grid, using a weighting of velocities by the particles transit time, to get rid of velocity biases as explained by Buchhave *et al.* (1979). This acquisition mode does not have a constant acquisition rate, so we use a different method for the acquisition of well-sampled signals to perform temporal analysis at single points. In this so-called dead-time mode, we ensure an average data rate of approximately 5 kHz, and the Burst Spectrum Analyzer takes one sample every single millisecond such that the final data rate is 1 kHz. For practical reasons, this method is well-suited for points close to the cylindrical wall, so we choose the point $\{r = 0.9 ; z = 0\}$ for the measurements in figures 7, 8 and 10 of §4. The

signals are resampled at 300Hz by a ‘‘Sample And Hold’’ algorithm (Buchhave *et al.* 1979).

Let us now consider the experimental error on the Reynolds number value. The speed servo-loop control ensures a precision of 0.5% on f , and an absolute precision of ± 0.002 on the relative difference of the impellers speeds $(f_2 - f_1)/(2f)$. The main error on the Reynolds number is thus a systematic error that comes from the estimation of the viscosity. As far as the variation of the viscosity with temperature is about 4% for 1°C and the variation with concentration is about 5% for 1% of mass concentration, we estimate the error on Re to be $\pm 10\%$ (the temperature is known within 1°C). However, the experimental reproducibility of the Reynolds number is much higher than $\pm 10\%$. In the range $100 \lesssim Re \lesssim 500$ we are able to impose Re within ± 5 .

3. Viscosity dominated steady states at low-Reynolds number

We describe here the basic flow state and the first bifurcated mode, in the range $30 \lesssim Re \lesssim 300$.

3.1. Basic state

We focus on the negative direction of rotation ($-$) in a first time. At very low-Reynolds number, the basic laminar flow respects the symmetries of the problem. It is stationary, axisymmetric and \mathcal{R}_π -symmetric. This state is stable at $Re = 90$, where we present a flow visualisation in figure 3(a-b). In figure 3(a), the light sheet passes through the axis of the cylinder. The visualised velocities are the radial and axial components. The poloidal part of the flow consists of two toric recirculation cells, with axial pumping directed to the impellers.

The flow is also made of two counter-rotating cells, separated by an azimuthal flat shear-layer, which can be seen in figure 3(b) where the light sheet is quasi-tangent to the cylinder wall. Both the azimuthal and axial component vanishes in the plane $z = 0$ which is consistent with the axisymmetry and the \mathcal{R}_π -symmetry. This flat shear-layer is sketched in figure 3(e).

3.2. First instability

The first instability for this flow has been determined by visualisation and occurs at $Re = 175 \pm 5$ for both directions of rotation. The bifurcation is supercritical, non-hysteretic, and leads to a stationary regime, with an azimuthal modulation of $m = 2$ wave number. We present a visualisation of this secondary state in figure 3(c), at $Re = 185$. The axisymmetry is broken: one can see the $m = 2$ modulation of the shear-layer, also sketched in figure 3(e). One can also note that \mathcal{R}_π -symmetry is partly broken: the bifurcated flow is \mathcal{R}_π -symmetric with respect to two orthogonal radial axis only. This first instability is very similar to the Kelvin–Helmholtz instability. Nore *et al.* (2003) made a proper theoretical extension of the Kelvin–Helmholtz instability in a cylinder. Their model is based on the use of local shear-layer thicknesses and Reynolds numbers to take into account the radial variations in the cylindrical case.

3.3. Evolution of the torque

The flow is laminar for these two modes. The viscous terms are thus dominant in the momentum balance such as at constant viscosity the torque on the impellers is proportional to the impellers frequency for low values of Re , as shown in figure 4. In addition, we plot in figure 5 the dimensionless torque K_p as a function of the Reynolds number,

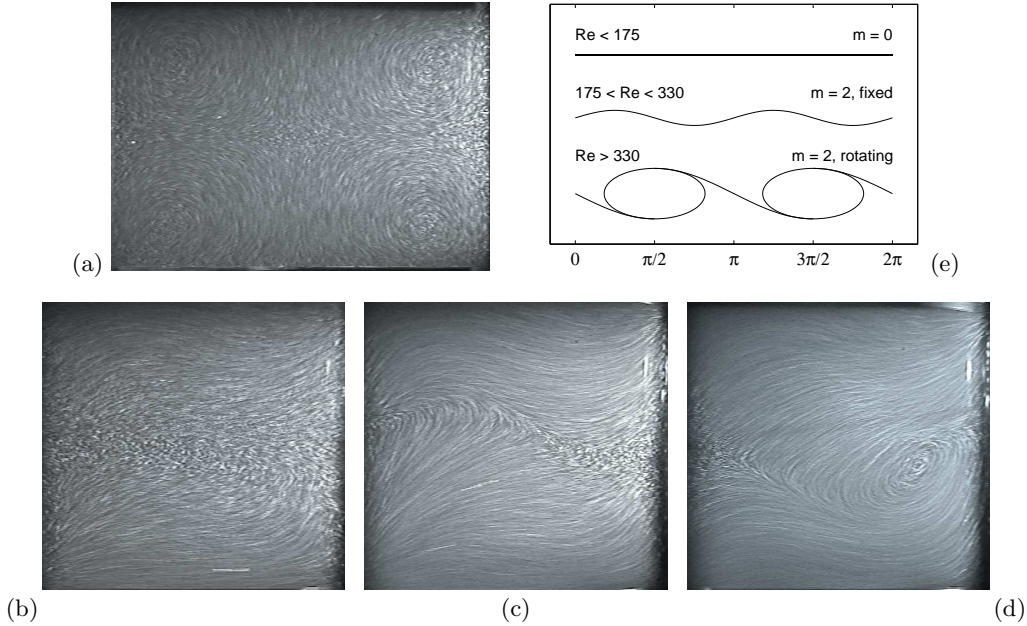


FIGURE 3. Visualisation and schematics of the basic laminar flow for impellers rotating in direction $(-)$. The lightning is made with a vertical light sheet. Pictures are integrated over $1/25$ s with a video camera, and small air bubbles are used as tracers. Laminar axisymmetric flow at $Re = 90$, meridian view (a). Views in a plane near the cylinder wall at $Re = 90$ (b), $Re = 185$ (c) and $Re = 345$ (d). The development of the first $m = 2$ instabilities—steady undulation (c) and rotating vortices (d)—is clearly visible on the shape of the shear-layer. We give sketches of the shear-layer for these Reynolds numbers in (e).

for all the experiments we performed. This quantity scales as Re^{-1} in the laminar regime (Schlichting 1979).

Increasing further the Reynolds number, the flow stays laminar almost until $Re \simeq 300$, where the dimensionless torque starts to shift from a Re^{-1} law (see fits and captions in Figs. 4 and 5). Until right now, we have chosen to emphasize one direction of rotation, namely $(-)$, for the presentation of the basic states. We also study the direction $(+)$ (see figure 1b), which at high-Reynolds numbers leads to a different mean flow, and to a three times weaker power consumption (Ravelet *et al.* 2005). A surprising result is that at low Re , the two directions of rotations are equivalent as can be seen in figure 5. The two curves (circles for direction $(-)$ and left triangles for direction $(+)$) collapse for $Re \lesssim 300$ on a single curve of equation $K_p = 36.9Re^{-1}$ and separates after this laminar regime where viscous terms dominate the momentum balance equation. We performed velocity field measurements for the two flows at $Re \simeq 120$. We present them in figure 6(c-f). At first order, no differences between the two directions are evidenced. The order of magnitude of the mean poloidal and toroidal velocities are the same for both directions of rotation in the laminar regime, whereas at very high Re , they strongly differ (Ravelet *et al.* 2005).

3.4. From viscous to inertial stirring

The flow is thus not sensitive to the shape of the impeller blades in the laminar regime. We make the hypothesis that for these large impellers of radius $0.925R_c$, fitted with blades of height $h = 0.2R_c$, the flow at low Re is equivalent to the flow between flat disks in an effective aspect ratio $\Gamma = (H - 2h)/R_c = 1.4$. Nore *et al.* (2004) numerically studied

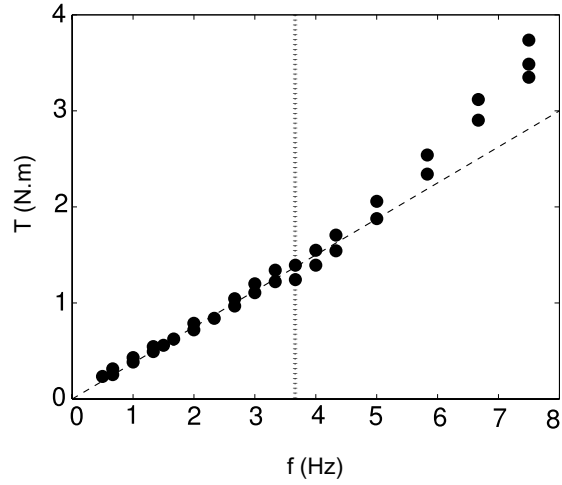


FIGURE 4. Dimensional Torque T vs. rotation frequency f , with 99%-pure glycerol at 16°C for impellers rotating in direction (-). The vertical line corresponds to $Re = 300$. Dashed line is a linear fit: $T = 0.38f$ (fitted below $f = 3.5$ Hz).

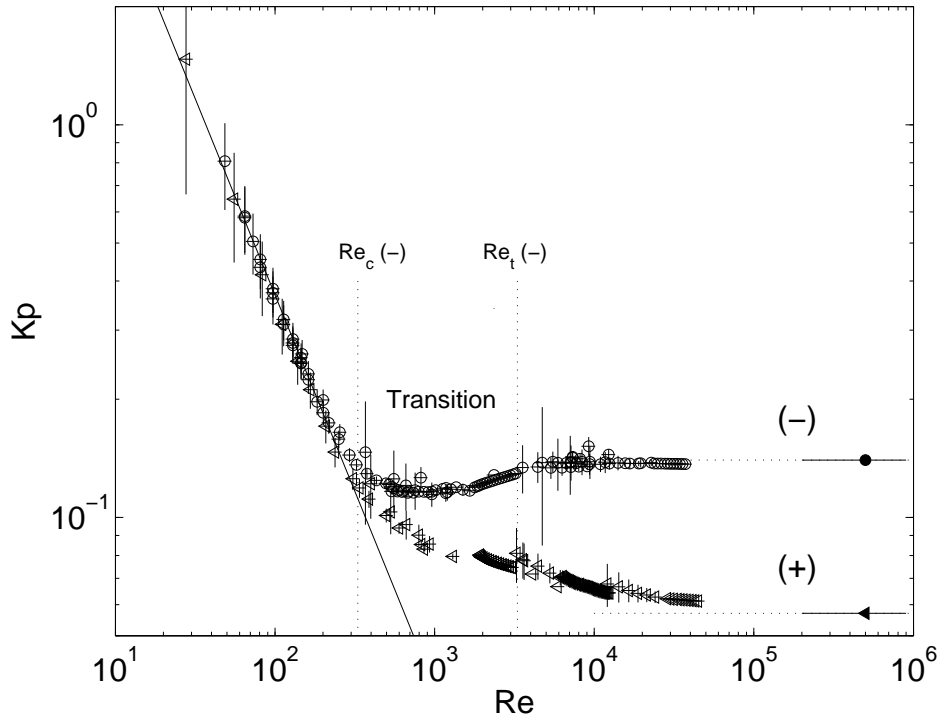


FIGURE 5. Dimensionless torque K_p vs. Re in a log-log scale. (o) : direction of rotation (-). (\triangleleft) : direction of rotation (+). Relative error on Re is $\pm 10\%$; absolute error of ± 0.1 N.m on the torque. The solid line is a nonlinear fit of equation $K_p = 36.9 \times Re^{-1}$ between $Re = 30$ and $Re = 250$. Re_c and Re_t are the transition values computed from the fits of figure 10. The single points, displayed at $Re = 5 \times 10^5$, correspond to measurements in water, where K_p is extracted from a fit of the dimensional torque in $a + b \times f^2$ for $2 \times 10^5 \lesssim Re \lesssim 9 \times 10^5$ (Ravelet *et al.* 2005).

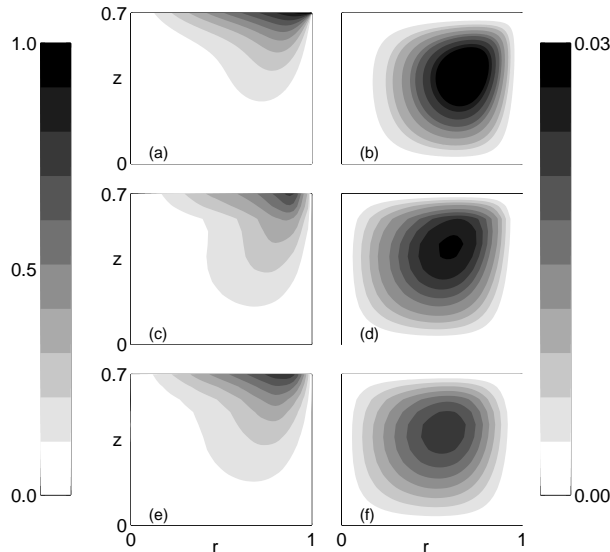


FIGURE 6. Comparison between a numerical simulation (a-b) performed with the code of Nore *et al.* (2003) in a cylinder of aspect ratio $\Gamma = 1.4$ at $Re = 120$ and two experimental velocity fields measured by LDV in direction (+) at $Re = 130$ (c-d) and in direction (-) at $Re = 120$ (e-f). The flow quantities which we present are in (a-c-e) the azimuthal velocity v_θ and in (b-d-f) the poloidal stream function Ψ . Presenting the fields between $0 \leq r \leq 1$ and $0 \leq z \leq 0.7$ is sufficient due to axisymmetry and \mathcal{R}_π -symmetry. Blades or smooth disk are at $z = 0.7$.

the flow between counter-rotating smooth flat disks enclosed in a cylinder and report the dependence of the first unstable mode wave number on the aspect ratio $\Gamma = H/R_c$. In their computations, the critical wave number is $m = 1$ for $\Gamma = 1.8$, whereas for $\Gamma = 1.4$, it is $m = 2$ as we do observe in our experiments.

We thus compare our experimental velocity fields to a numerical simulation performed at the same Re and in aspect ratio $\Gamma = 1.4$ in figure 6. The three fields are very close. A possible physical explanation for this effect is the presence of viscous boundary layers along the resting cylinder wall. The typical length scale of the boundary layer thickness can be estimated as $\delta = Re^{-1/2}$. At the Reynolds number when the impellers blades start to become visible, *i.e.* at $Re \simeq 300$, this boundary layer thickness is of the order of $\delta \simeq 6$ mm, while the gap between the impellers and the cylinder wall is 7.5 mm. It is also of the order of magnitude of the minimum distance between impeller blades. For $Re \lesssim 300$, the fluid is thus kept between the blades and can not be expelled radially: it rotates solidly with the impellers. The stirring cannot be considered as inertial and does not depend on the blades shape.

For Reynolds numbers higher than 300, the inertial stirring becomes dominant. Also, in this Reynolds number range, the secondary mode —an azimuthal $m = 2$ stationary mode below $Re = 300$ — becomes unstable with respect to time-dependence.

4. A globally supercritical transition to turbulence

This section is devoted to the study of time-dependence from the laminar regime up to the transition to turbulence. Since the stirring is inertial and the blades are curved, the dynamics is different for the two directions of rotation. We now restrict our study to impellers rotating in the negative direction (circles in figure 5).

Around $Re \simeq 300$, the flow is characterized by a laminar $m = 2$ shear-layer which

breaks the initial axisymmetry. In addition to visualisations we perform precise velocity measurements at a given point in this layer. We measure the azimuthal component v_θ at $\{r = 0.9 ; z = 0\}$, using the dead-time acquisition mode (see § 2). This section is divided into two subsections. In a first subsection, we describe the observed dynamics and how the chaotic and turbulent spectra build up. In the second subsection, we draw quantitative data about the dynamical regimes, we discuss the mechanisms and we propose a global view of the transition to turbulence.

4.1. Some states encountered on the route to turbulence

4.1.1. From quasi-periodicity to chaos: the low-frequency spectrum

We present time series of the velocity and their power spectral densities at three Reynolds numbers in figure 7: $Re = 330 \pm 5$, $Re = 380 \pm 5$ and $Re = 440 \pm 5$.

The point at $Re = 330 \pm 5$ is the first point where a clear temporal dynamics is observed: a sharp peak in the spectrum (figure 7b) is present at the impeller rotation frequency $f_a = f$ —emphasized in the Inset of figure 7(a)— and some energy is also localized at low frequency around $f_a \simeq f/30$. In comparison, a similar measurement performed at $Re \simeq 260$ reveals a flat signal with a very low flat-spectrum with just a tiny peak —1/1000 of the amplitude measured at $Re = 330$ — at $f_a = f$. On the long time series at low Re (figures 7a, c and e), the high-frequency oscillation at the impeller frequency is too fast to be explicitly visible but is responsible for the large width of the signal line.

In figure 7(a) the mean velocity is not zero, but almost constant around $v_\theta = +0.17$ during the 600 time units of acquisition, *i.e.*, during 600 disks rotations. This value of the velocity has no special meaning and depends on the phase between the shear-layer and the measurement point. The measurement point indeed stays on the same side of the shear-layer. Yet, on much longer time scales, we observe the shear-layer to rotate slowly in a given direction with a typical time scale of $5000f^{-1}$. This corresponds still to a very low frequency, of the order of the dissymmetry of the speed servo loop control between both independent motors, see § 2.2. This is probably the limit of the symmetry of our system: on the visualisations at $Re \simeq 190$ and $Re \simeq 230$, a similar shift in the same direction of the $m = 2$ shear-layer has been monitored (see discussion in § 5.1).

For $330 < Re < 400$ the velocity signal is quasi-periodic. This is illustrated at $Re = 380$ in figure 7(c-d). The mean velocity is now zero: the shear-layer rotates slowly such that the measurement point is alternatively in the cell rotating with the upper impeller ($v_\theta > 0$) and in the cell rotating with the lower impeller ($v_\theta < 0$). Visualisations confirm that this corresponds to a propagating wave and also show that the $m = 2$ shear-layer is now composed of two vortices (figure 3d) and thus deserves the term “mixing-layer”. Along the equatorial line, one notice that the parity is broken (as defined in Coulet & Iooss 1990). The velocity varies between $-0.3 \lesssim v_\theta \lesssim 0.3$. The wave oscillation is slow but one order of magnitude faster than the drift described above: one can see two periods during 600 time units, *i.e.* a frequency of $f/300$ which is very difficult to resolve by spectral analysis owing to the shortness of the signal (*cf* caption of figure 7). At $Re = 380$ (figure 7c-d), the peak at the rotation frequency is still present, but starts to spread and becomes broadband. The power spectral density at frequencies higher than $3f$ decreases extremely rapidly to the noise level. Let us note that \mathcal{R}_π -symmetry remains only with respect to a pair of orthogonal radial axis which rotates with the propagating wave.

The upper limit of the quasi-periodic regime is $Re = 400 \pm 5$. Above this threshold, the dynamics of the mixing-layer becomes chaotic: the velocity signal (see figure 7e) at $Re = 440$ can be described as series of almost random jumps from one side to the

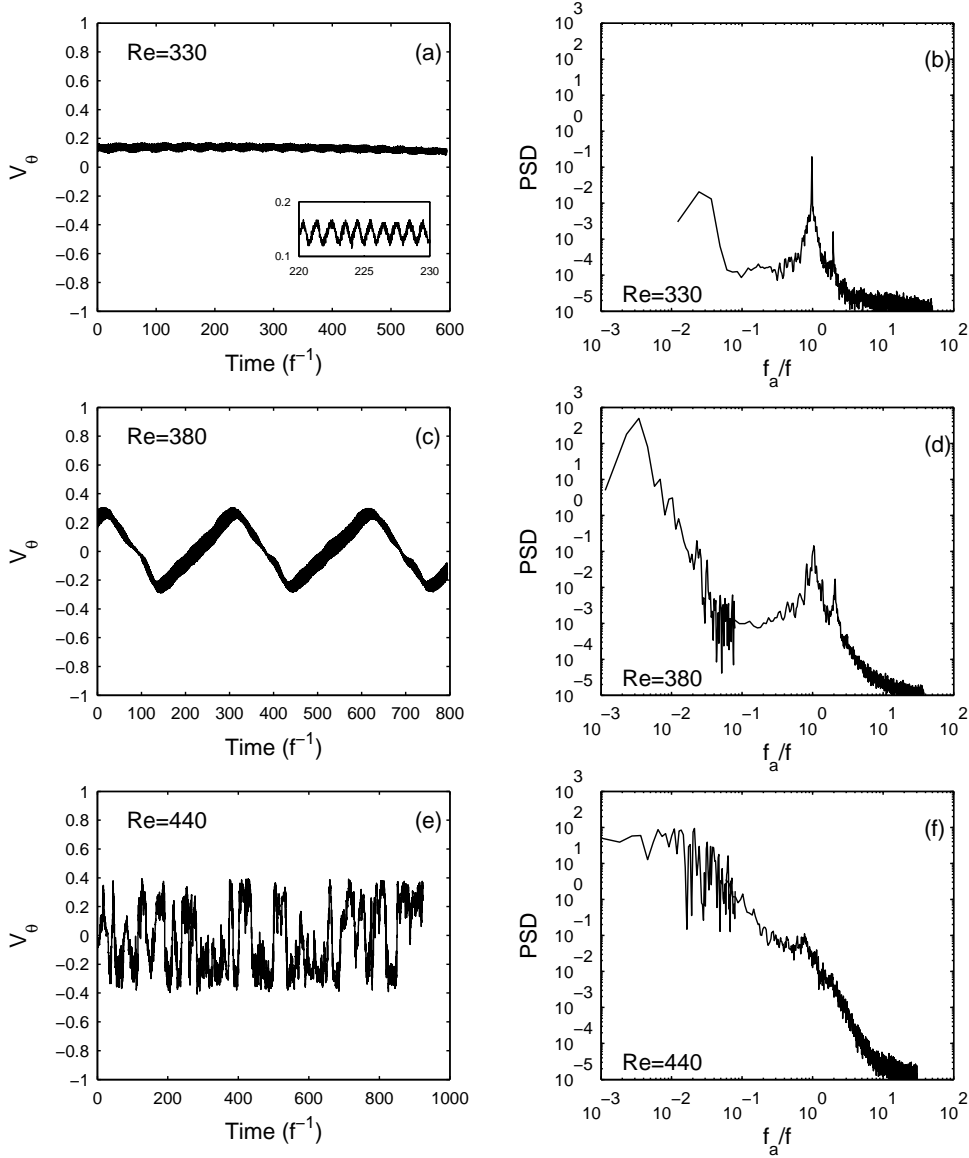


FIGURE 7. Temporal signal $v_\theta(t)$ measured by LDV at $\{r = 0.9 ; z = 0\}$ and power spectral density (PSD), at: (a-b) $Re = 330$, (c-d) $Re = 380$ and (e-f) $Re = 440$. f_a is the analysis frequency whereas f is the impellers rotation frequency. The Inset in (a) is a zoom over the fast oscillation at frequency f . In order to improve the signal to noise ratio for the 4 to 5 decades spectra, we compute the power spectrum by the Welch periodogram method twice: first with a very long window to catch the slow temporal dynamics; second with a shorter window, to reduce fast scales noise by averaging. We then plot together the lower part of the first spectrum and the higher part of the second one.

other side of the $v = 0$ axis. The peaks reached by the velocity are now in the range $-0.4 \lesssim v_\theta \lesssim 0.4$. The alternate changeover between the two counter-rotating cells is moreover “chaotic” and involves more or less long stays in one side followed by very fast transitions to the other side of the mixing-layer.

From the visualisations, we observe that the $m = 2$ symmetry is now broken. The mixing-layer vortices, which are still globally rotating around the cell in the previous direction, also behave more and more erratically with increasing Re : their individual dynamics includes excursions in the opposite direction as well as towards one or the other impeller.

The spectral analysis of the signal at $Re = 440$ (figure 7f), does not reveal any well-defined frequency peak anymore. However, a continuum of highly-energetic fluctuations at low frequency, below $f_a = f$ and down to $f_a = f/100$, emerges. A small bump at the rotation frequency f is still visible, and a region of fast fluctuations above the injection frequency also seems to arise.

4.1.2. From chaos to turbulence: the high-frequency spectrum

Increasing further the Reynolds number, one obtains the situation depicted in figure 8. The slow dynamics which could be thought as depending only on the largest spatial scales of the flow is well built above $Re \simeq 10^3$. The velocities corresponding to the two cells at $Re = 1.0 \times 10^3$ and above (figures 8a, c and g) are of the order of ± 0.6 . The power spectral density below the injection frequency seems to behave with a f^{-1} power-law over two decades for these two Reynolds numbers (figure 8b-d). The spectral density saturates below $10^{-2}f$.

Concerning the fast time scales, which are usually interpreted as a trace of small spatial scales fluctuations, one can see some evolution between $Re = 1.0 \times 10^3$ and $Re = 6.5 \times 10^3$. At the former Reynolds number, there are few fast fluctuations which decay faster than $f^{-5/3}$ and the intermittent changeovers are easy to identify in the temporal signal in figure 8(a). At the latter Reynolds number, the fast (small scales) fluctuations are bigger and almost behave with a $f^{-5/3}$ law (figure 8h).

We want to emphasize that in such a closed flow with no net mean flow at the point we have chosen and with fluctuations of the order of the mean kinetic energy, the Taylor hypothesis is not suited (Lumley 1965) and that one should not *a priori* interpret time spectra as space spectra Pinton & Labbé (1994) (see discussion in § 5.2.2).

4.2. Quantitative characterization of the transitions

Since the various dynamic states encountered have been described and illustrated in the previous subsection, we now wish to address the question of the nature of the transitions.

4.2.1. From order to chaos

Our diagnostic is mainly based on two properties of the velocity signal: the amplitude of the velocity fluctuations along time and their main frequency. In the quasi-periodic regime, even if only few periods are monitored along single time-series, we carefully estimate the period by measuring the time delay between crossings of the $v = 0$ axis. These value are reported of figure 9(a) with closed circles. In an equivalent way, the periodicity of the travelling of the mixing-layer vortices on the visualisations give complementary data, represented by closed squares on the same figure.

The main result is obvious: the quasi-periodic low-frequency f_{QP} behaves linearly with Re above a threshold Re_{QP} very close to 330. Both measurement methods agree even if the visualisations deserves large error bars in Re at least due to the shortness of our records and to a poorer thermal control. Fit is made on velocity data only. We observe some level of imperfection in the quasi-periodic bifurcation, due to the pre-existing drift below f_{QP} which we believe to be related to small differences between both impeller frequencies. In fact we observe on our movies the mixing-layer to start rotating along the drift direction.

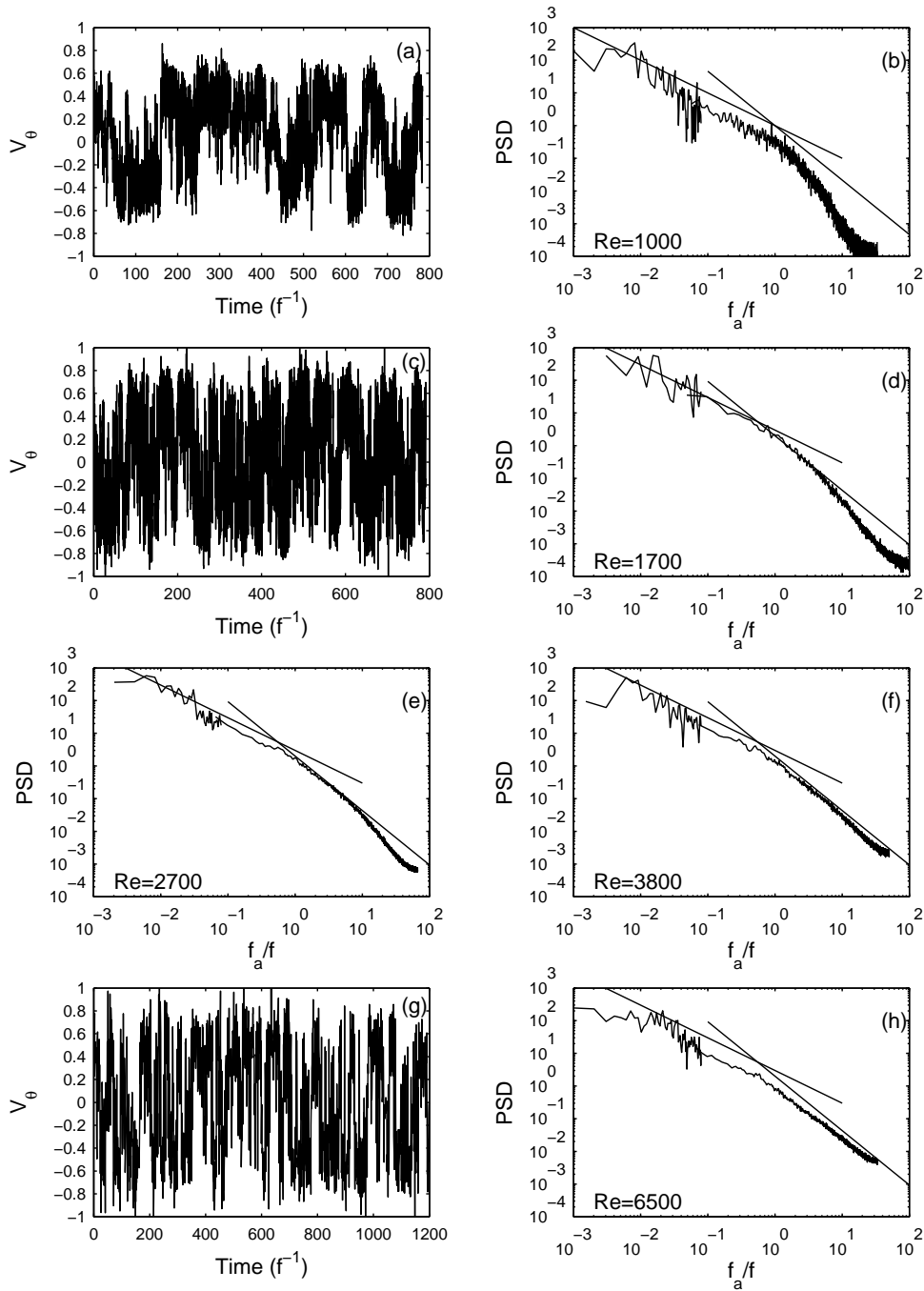


FIGURE 8. (a-b): Temporal signal $v_\theta(t)$ measured by LDV at $\{r = 0.9; z = 0\}$ and power spectral density at $Re = 10^3$. (c-d): Temporal signal and power spectral density at $Re = 1.7 \times 10^3$. (e-f): Power spectral densities at 2.7×10^3 and 3.8×10^3 . (g-h) Temporal signal and power spectral density at 6.5×10^3 . Solid lines in the power spectra plots are power-law eye-guides of slope -1 and $-5/3$. Spectra are computed as explained in the caption of figure 7.

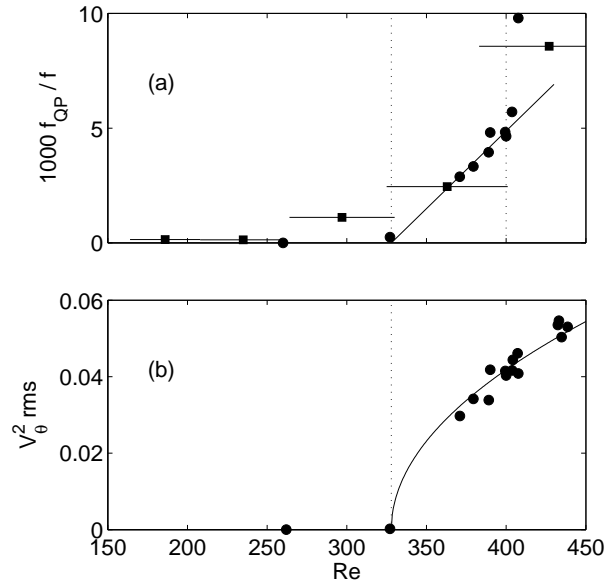


FIGURE 9. (a) Low-frequency f_{QP} of the quasi-periodic regime of velocity $v_\theta(t)$ measured at $\{r = 0.9 ; z = 0\}$ (closed circles) and drift frequency of the $m = 2$ shear-layer pattern from flow visualisations (closed squares). The solid line is a linear fit of f_{QP} between the two thresholds $Re_{QP} = 330$ and $Re_{chaos} = 400$, indicated by vertical dotted lines. (b) Variance of $v_\theta(t)$ measured at $\{r = 0.9 ; z = 0\}$ vs. Re : zoom of figure 10.

The amplitude can be monitored by computing the evolution of the kinetic energy fluctuations, i.e., the variance $v_\theta^2_{rms}$ of the LDV-time-series. This method allows considering altogether the broadband frequency response of the signal (see below). The variations of $v_\theta^2_{rms}$ due to the drift below onset, which appear very small in figure 7(a), can be estimated as typically 0.01. Data are plotted in figure 9(b) together with the fit in $(Re - Re_c)^{1/2}$ which will be discussed below. Both fits on amplitude and frequency converge to exactly the same threshold $Re_{QP} = Re_c = 328$.

We conclude that the quasi-periodic mode bifurcates at $Re = 330 \pm 5$. We believe that both peaks at $f_a = f$ and $f_a = f_{QP}$ appear together through respectively a finite-frequency type-I₀ bifurcation for f and a zero-frequency type-II₀ bifurcation for f_{QP} (Cross & Hohenberg 1993). However, we did not carry highly Reynolds-number resolved observations below $Re = 330$ and it cannot be excluded that the f -peak appears alone first between $Re = 260$ and Re_{QP} .

The transition to chaos is observed for $Re > Re_{chaos} = 400 \pm 5$. There is no hysteresis. Very close to the chaotic threshold, the signal sometimes exhibits a few almost-quasi-periodic oscillations still allowing us to measure a characteristic frequency. The measured values have been also plotted on figure 9(a) and are clearly above the linear fit and could reveal a vanishing time scale, i.e., a precursor of the very sharp positive/negative jumps of v_θ reported in the chaotic and turbulent regimes. In a narrow region around the chaotic transition, i.e., between $Re = 389$ and $Re = 408$, we also notice on the signal a fast oscillation mode —not visible on the presented figures— at frequency $f/(6.2 \pm 0.2)$, independent of Re .

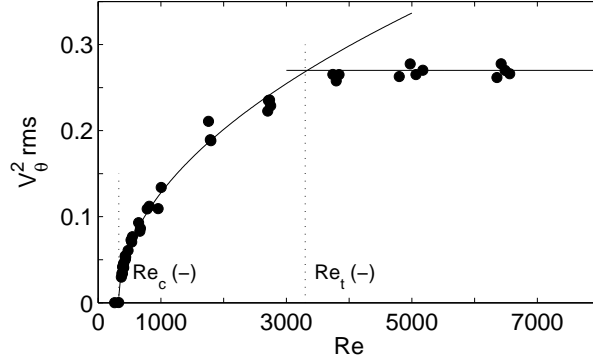


FIGURE 10. Variance of $v_\theta(t)$ measured at $\{r = 0.9 ; z = 0\}$ vs. Re . Solid line: nonlinear fit of the form $v_{\theta \text{ rms}}^2 = a \times (Re - Re_c)^{1/2}$, fitted between $Re = 350$ and $Re = 2500$. The regression coefficient is $R^2 = 0.990$, and the fit gives $Re_c = 330$. The intersection between this fit and the asymptotic value $v_{\theta \text{ rms}}^2 \simeq 0.27$ gives $Re_t = 3.3 \times 10^3$.

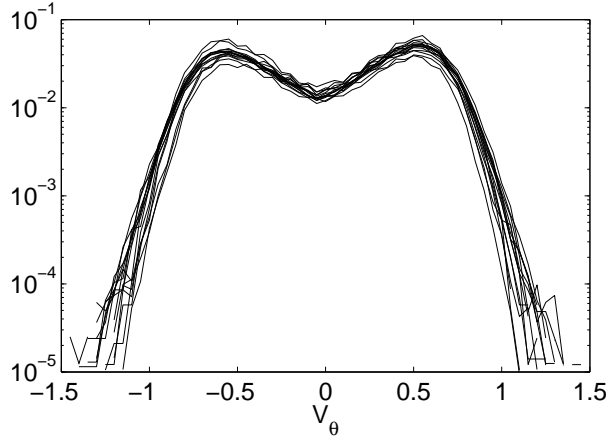


FIGURE 11. Probability density function (PDF) of v_θ for 16 Reynolds numbers in the range $2.5 \times 10^3 \lesssim Re \lesssim 6.5 \times 10^3$.

4.2.2. From order to turbulence

It is known that fully turbulent von Kármán flow can generate velocity fluctuations of typically 50% of the driving impellers velocity. So, we compute the variance $v_{\theta \text{ rms}}^2$ of the LDV-time-series at the measurement point *versus* the Reynolds number. This quantity is homogeneous to a kinetic energy and may be referred to as the azimuthal kinetic energy fluctuations. The results are reported in figure 10 for all the measurements performed between $260 \lesssim Re \lesssim 6500$. This curve quantitatively characterizes the transition to turbulence once the time-dependent regimes are reached. A puzzling feature is that this quantity—the kinetic energy of the fluctuating azimuthal velocity at one point—behaves like an order parameter for a standard supercritical bifurcation. This quantity can be fitted with a law in the square root of the distance to a threshold Re_c (figure 10), using data between $Re = 350$ and $Re = 2500$. Even more puzzling, this threshold is found to be $Re_c = 330$ and coincides with the onset of quasi-periodicity as detected on the variation of the low-frequency on the quasi-periodic signal (see above).

The $(Re - Re_c)^{1/2}$ behaviour can be fitted through the quasi-periodic and chaotic

regimes, up to $Re \sim 3000$. There, the azimuthal kinetic energy fluctuations level saturates at $v_{\theta}^2_{rms} \simeq 0.27$, *i.e.* fluctuations of velocities at this point of the mixing-layer are of the order of 50% of the impeller tip speed. This saturation is also revealed by the Probability Density Functions (PDF) of v_{θ} presented in figure 11. These PDF are computed for 16 Reynolds numbers in the range $2.5 \times 10^3 \lesssim Re \lesssim 6.5 \times 10^3$. One can notice the bimodal character of the PDF: the two bumps, which are symmetric, correspond to the two counter-rotating cells. Furthermore, all these PDF collapse and are therefore almost independent of Re in this range. This is also consistent with the spectral data of figure 8(b-d) where the $(f_a/f)^{-1}$ slowest time-scales regions which contain most of the energy — below f — appear similar for $Re = 1.0 \times 10^3$ and above (figure 8). The crossover Reynolds number Re_t at which the kinetic energy of fluctuations saturates in figure 10 is estimated by taking the intersection of the horizontal asymptote with the fit: $Re_t = 3.3 \times 10^3$. This value corresponds precisely to the value where the asymptotic plateau is reached in the K_p vs. Re diagram (figure 5). In such an inertially-driven turbulent flow, the bulk dissipation is much stronger than the dissipation in boundary layers and the global dimensionless quantities thus do not depend on the Reynolds number past a turbulent threshold (Lathrop *et al.* 1992; Cadot *et al.* 1997). In our experiment, a plateau is clearly reached in the negative sense for $Re \gtrsim Re_t = 3.3 \times 10^3$, whereas in the positive sense of rotation, some logarithmic corrections are still observed on the variation of K_p in the range $10^4 \lesssim Re \lesssim 5 \times 10^4$.

Finally, looking at the time-spectra above Re_t (figure 8f-h), we observe a completely developed power-law domain with $-5/3$ slope at high-frequency for $f_a > f$. This behaviour reminds the Kolmogorov $k^{-5/3}$ classical energy cascade (see discussion below). Furthermore, this $-5/3$ slope power-law domain is observed to build up progressively between $Re \simeq 1000$ and Re_t (figure 8a-e).

From the above reported observations, we conclude that the transition to turbulence is completed at Re_t for the negative direction of rotation and that the azimuthal kinetic energy fluctuation can clearly be considered as an order parameter for the whole transition, from the onset of time-dependence $Re_c = Re_{QP} = 330$ to the fully turbulent state transition/crossover at $Re_t = 3.3 \times 10^3$, *i.e.*, over a decade in Reynolds number.

The last experimental question we wish to address concerns the transition or the crossover between chaos and turbulence for $Re \simeq 1000$. It seems to be no evidence of any special sign to discriminate between the two regimes. An empirical criterion we could propose would be the completeness of the $(f_a/f)^{-1}$ low-frequency part of the spectrum, clearly achieved for $Re = 1000$ (figure 8b). This region also corresponds to the minimum of the $K_p(Re)$ curve (figure 5). One can propose that below this Reynolds number, the power injected at the impeller rotation frequency mainly excites low frequencies belonging to the “chaotic” spectrum, whereas above $Re \simeq 1000$ it also drives the high frequencies through the Kolmogorov-Richardson energy cascade.

The minimum of $K_p(Re)$ near $Re \simeq 10^3$ (circles in figure 5) was difficult to make clear experimentally because of the dispersion of data collected at different glycerol concentrations, different speed and different temperatures. To obtain a precise profile of the curve in this region, we measured the torque in a single run at fixed impeller speed without temperature regulation (figure 12). The fluid warms up gently during the run, from $T \simeq 16^\circ\text{C}$ to $T \simeq 31^\circ\text{C}$, and the Reynolds number evolves from $Re \simeq 820$ to $Re \simeq 2700$. The torque indeed decreases first and then increase, confirming the non-monotonic behaviour of the dimensionless torque in this Reynolds number range (density variation is neglected).

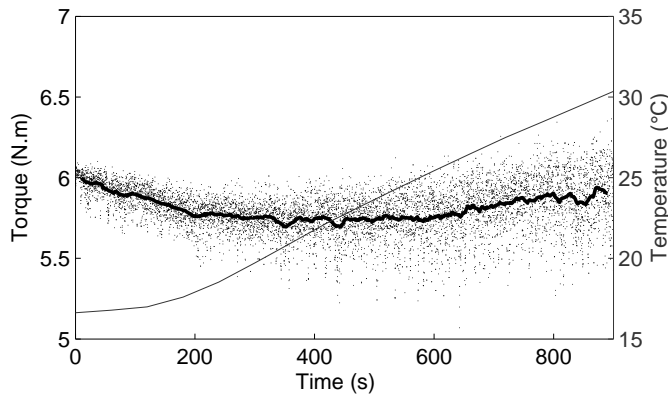


FIGURE 12. Time evolution of the torque (experimental point and gliding average) and of the temperature (thin line) without temperature regulation, for impellers rotating at -10 Hz, with 85% glycerol concentration. A data set is reported with respect to Re on figure 5.

5. Discussion

Before entering our discussion, let us summarize the observed steps revealed by our analysis on the supercritical route to turbulence in the von Kármán flow with inertial stirring:

- $Re < 175$: $m = 0$, axisymmetric, full \mathcal{R}_π -symmetric steady basic flow,
- $175 < Re < 330$: $m = 2$, discretely \mathcal{R}_π -symmetric steady flow,
- $330 < Re < 400$: $m = 2$, non \mathcal{R}_π -symmetric, equatorial-parity-broken quasi-periodic flow,
- $400 < Re \lesssim 1000$: chaotic flow,
- $1000 \lesssim Re \lesssim 3300$: transition to turbulence,
- $Re \gtrsim 3300$: inertially-driven fully turbulent flow.

Although this list as well as the previous section of the paper concerns only the case of negative rotation of the impellers, some aspect of the forthcoming discussion will also invoke the other rotation direction which has not been especially studied with the same point of view. Some complementary results can be found in (Marié *et al.* 2003; Ravelet *et al.* 2005; Monchaux *et al.* 2006b).

5.1. Symmetries and first bifurcations

The similarity of the behaviour of the flow at low-Reynolds number with intermediate-size nonlinear system is obvious: breaking a spatial symmetry first, then a temporal symmetry and finally transit to chaos by a quasi-periodic scenario.

Comparable study has been carried both experimentally and numerically in the von Kármán flow with flat disk and variable aspect ratio by Nore *et al.* (2003, 2004, 2005). Our results agree well with their results on the first instability mode $m = 2$ if considering the fluid in the blade region as almost solidly driven, which reduces the aspect ratio. However, all thresholds appear at much lower Re for bladed impellers than for flat disks: 175 *vs.* 300 for the first steady bifurcation and 330 *vs.* more than 600 for the first temporal instability of $m = 2$ mode, not observed in Nore *et al.* (2005) study.

Another important difference between both system concerns its symmetries. Whereas Nore and collaborators deal with exact counter rotation by using a single motor to drive both disks, our experimental setup uses two independent motors and reaches only a approximation on a counter-rotating regime. As a consequence, the \mathcal{R}_π -symmetry is *stricto sensu* broken at any Reynolds number and the group of symmetry of our problem is

$SO(2)$ instead of $O(2)$. So instead of non-rotating mixed modes, pure mode and heteroclinic cycles specific of $O(2)$ we only observe rotating instability patterns (Crawford & Knobloch 1991), i.e., traveling waves. Below $Re_c = 330$, the $m = 2$ pattern of the mixing-layer (figure 3c) rotates very slowly due to the frequency mismatch between both impeller. Above $Re_c = 330$, the parity of the pattern gets broken (figure 3d) and starts rotating faster and faster with Re (figure 9a). This bifurcation is similar to the 1-D drift instability of steady patterns related to the parity break (Coulet & Iooss 1990). Otherwise, the comparison of our traveling waves with those observed with flat disks (Nore *et al.* 2003, 2005) rises two comments: the frequencies are of the same order of magnitude, which let us believe that the same hydrodynamics is involved, whereas the bladed system superimposes an oscillation at the driving frequency f and the flat disks do not.

We also wish to consider the symmetry of the von Kármán flow with respect to the rotation axis. In fact, the time-averaged flow is exactly axisymmetric while the instantaneous flow is not because of the presence of blades. However, axisymmetry can be considered as an effective property at any time at low-Reynolds number and at least up to $Re = 175$, since we have shown that the blades have almost no effect on the flow (see §3.4). With increasing Re , the blades start playing their role and effectively break the axisymmetry of the instantaneous flow.

Finally, we emphasize that the observations made below $Re \sim 400$ closely remind the route to chaos through successive symmetry break for low degree of freedom dynamical systems. Our system can thus be considered as a small system—in fact this is coherent with the aspect ratio which is of order of 1—until the Reynolds number becomes high enough to excite small dynamical scales in the flow.

5.2. The three scales of the von Kármán flow

The observations reported in this article—visualisations, spectra—evidenced three different scales. In particular, time-spectra contain two time-frequency domains above and below the injection frequency $f_a = f$. Let us first make a rough sketch of the correspondence between temporal and spatial frequency scales of the whole flow:

- the smallest space-frequencies, at the scale of the vessel, describe the basic swirling flow due to the impeller and produce the intermediate frequency-range, i.e., the peak at $f_a = f$ in the time-spectrum;
- the intermediate space-frequencies due to the shear-layer main instabilities produce the lowest time-frequencies;
- the highest space-frequencies produce, of course, the highest temporal frequencies, i.e., the Kolmogorov region.

We can thus emphasize that there is a non-monotonic mapping between space- and time-frequencies, which definitively excludes the validity of Taylor’s hypothesis over the full range of the spectra.

5.2.1. The $1/f$ low-frequency spectrum

Once chaos is reached at $Re = 400$, a strong continuous and monotonic low-frequency spectrum is generated (Fig. 7f). In the chaotic regime below $Re \sim 1000$, the spectrum evolves to a neat -1 power law. Then, this part of the spectrum does not evolve anymore with Re .

Low-frequency -1 exponents in spectra are common and could be due to a variety of physical phenomena: so-called “ $1/f$ noises” have been widely studied, *e.g.*, in the condensed matter field (see for instance Dutta & Horn 1981).

For turbulent von Kármán flows driven by two counter-rotating impellers, this low time-scale dynamics has been already observed over at least a decade in liquid helium

by Zocchi *et al.* (1994) as well as for the magnetic induction spectrum in liquid metals (Bourgoin *et al.* 2002; Volk *et al.* 2006). However, experiments carried on a one-cell flow —without turbulent mixing-layer— did not show this behaviour (Marié 2003; Ravelet *et al.* 2004; Ravelet 2005). We therefore conclude that the $1/f_a$ -spectrum is related to the chaotic wandering of the mixing-layer. Once again, the mixing-layer slow dynamics dominates the whole dynamics of our system, from momentum transfer (Marié & Daviaud 2004) to the very high level of turbulent fluctuations (Fig. 10,11).

Furthermore, we can make the hypothesis that the -1 slope is due to the distribution of persistence times in each side of the bimodal distribution (Fig. 11). Similar study of the low-frequency spectral construction is currently under progress for the magnetic induction in the von Kármán sodium experiment. In both cases, longer statistics are needed to check this idea.

5.2.2. The turbulent fluctuations

We emphasize above how the flow transits from chaos to turbulence between $Re \simeq 1000$ and $Re_t = 3300$. We labeled this region “transition to turbulence” and observed the growth of a power-law region in the time-spectra for $f_a > f$. Does this slope trace back the Kolmogorov cascade in the space-spectra ?

As the classical Taylor hypothesis cannot apply to our full range spectrum, we follow the Local Taylor Hypothesis idea (Pinton & Labbé 1994) for the high-frequency part $f_a > f$. Whereas Pinton & Labbé (1994) did not apply their technique —using instantaneous velocity instead of a constant advection— to the extreme case of zero advection, we think it can be applied here owing to the shape of the azimuthal velocity PDF (figure 11). These distributions shows first that the instantaneous zero velocity is a quite rare event: a local minimum of the curve. The modulus of velocity spends typically 75% of the time between $1/2V_m$ and $3/2V_m$, where $\pm V_m$ are the positions of the PDF maxima. The sign of the advection has no effect on the reconstructed wavenumber. We can thus conclude that frequency and wavenumber modulus can be matched each other at first order by a factor equal to the most probable velocity $|V_m|$ or by the mean of $|v_\theta|$, both very close to each other. This approach is coherent with a binary view of the local turbulent signal jumping randomly between two opposite mean values, just as in turbulent flow reversal model of, e.g., Benzi (2005). Then, the high-frequency part of the spectrum is equivalent to the spectrum obtained by averaging the spectra of every single time-serie between jumps, while the low-frequency part is dominated by dynamics of the jumps themselves.

Owing to these arguments, we are convinced that an algebraic region dominates the high-frequency part of k -spectra above Re_t in the negative direction of rotation. Observed exponents are of the order of the Kolmogorov exponent $-5/3$, probably a little bit smaller in absolute value. Similar exponents are also encountered at other locations in the vessel with the same rotation. However, careful study by Marié (2003); Marié & Daviaud (2004) in positive direction at higher $Re \sim 10^6$ revealed smaller exponents, between -1 and -1.3 , depending of the velocity component considered. Exponent measurement and quantitative comparison with any kind of model is far out the scope of our present studies and should be undertaken with extreme care.

5.3. Inertial effects

The initial motivation to drive our experiment continuously from laminar to turbulent regimes was to get an overview of the transition to turbulence and to check the range where multistability exists (see next paragraph and Ravelet *et al.* 2004). A first surprise was the continuity and global supercriticality of this transition (figure 10), the central subject of this paper. Another surprise came from the importance of inertial effects and

from how they clearly discriminate both directions of rotation at both low- and high-Reynolds numbers (see §3.4 and figure 5). The figure 13 presents the same points as in figure 5 together with additional data for smooth disks and for the bifurcated state discussed thereafter in §5.4. The dimensionless torque K_p is approximately 30 times smaller for smooth disks than for bladed disks, and does not display a plateau at high-Reynolds number but a $Re^{-1/4}$ scaling law, as described by Cadot *et al.* (1997). It is tempting to compare our curve $K_p(Re)$ with the classical work of Nikuradse (1932, 1933) consisting in a complete and careful experimental data set about the turbulence in a pipe flow with controlled wall roughness. The data concern the friction factor — equivalent of K_p — measured over a wide range between $Re = 500$ and $Re = 10^6$, which is shown to strongly depend of the wall roughness above $Re \simeq 3000$. The wall roughness is made by controlled sand grains of diameter in the range $1/507$ to $1/15$ of the pipe radius, somewhat smaller than our blades height $h/R_c = 1/5$ which can be thought as an effective roughness.

This data set has defied theory along decades and still motivates papers. Recently, Goldenfeld (2006) and Gioia & Chakraborty (2006) proposed phenomenological interpretations and empirical reduction of Nikuradse’s data. In few words, both recent works connect the very high-Reynolds inertial behaviour —a plateau at a value which scales with the roughness to the power $1/3$ — to the Blasius $Re^{-1/4}$ law for the dissipative region at intermediate Re . Goldenfeld (2006), using a method from critical point physics, finds a scaling for the whole domain above $Re \simeq 3000$, whereas Gioia & Chakraborty (2006) describe the friction factor over the same Reynolds range according to Kolmogorov’s phenomenological model.

Compared with pipe flow results and models, our $K_p(Re)$ -curve (figures 5 and 13) looks very similar except for the region Gioia & Chakraborty (2006) call the energetic regime. Indeed, in our specific case the basic flow itself is already dominated by vortices of the size of the vessel. The two directions of rotation have quite different behaviours. The negative direction (circles in figures 5 and 13) shows a minimum followed by a plateau above $Re_t = 3300$ and is in agreement with the general inertial behaviour described above. However for the positive direction (left triangles in figure 5), the K_p curve seems continuously decreasing up to $Re \simeq 10^6$. Looking closer, one can observe a short $Re^{-1/4}$ Blasius regime for Re between 300 and 1500 —highlighted by a fit in figure 13— followed by a very slow variation over the next two decades. For this direction it is more difficult to define a threshold for the expected plateau we observe in pure water (Marié 2003). Nevertheless, this threshold should be greater than 10^5 , *i.e.*, much higher than with negative rotation.

A possible explanation of this strong difference may rely in the structure of the flow inside the impellers, *i.e.* in-between the blades. Let us first assume that this flow is dominated by what happens along the extrados of the blades, on which the pressure is the higher. Then we can assume that the blades curvature leads to stable boundary layers in positive rotation and to Goertler instability in negative rotation. The first case develops Blasius boundary layers, whereas the latter develops turbulent boundary layers with much more vortices. Therefore, when the boundary layer detaches —somewhere along the blades or at least at their end— the Blasius boundary layer in the positive rotation sheds less turbulent vortices than the Goertler’s instable layer does in the negative rotation.

The above description can be sufficient to explain why the negative rotation is able to produce a strong Kolmogorov cascade even at quite low-Reynolds numbers near Re_t . However if, in the positive rotation case, the flow is only seeded by vortices produced by the stable boundary layer which develops along the smooth blade faces, it is clear that a Blasius $Re^{-1/4}$ can be observed in this transition Reynolds range and that a full

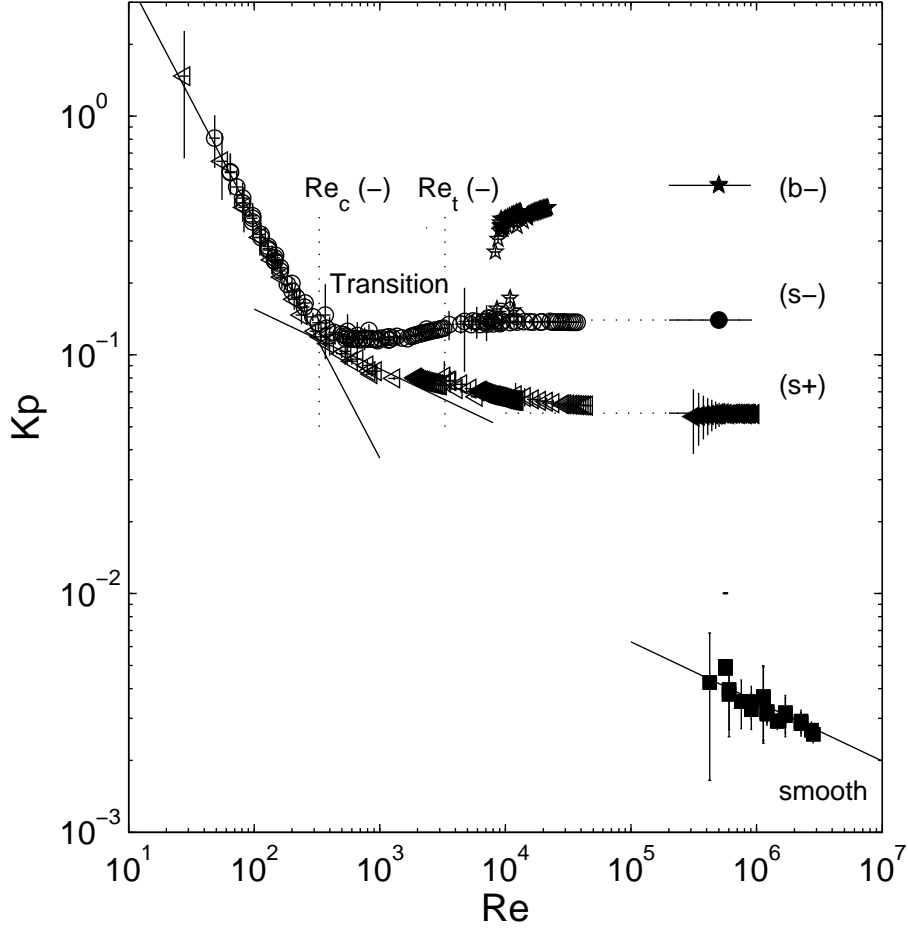


FIGURE 13. Compilation of the dimensionless torque K_p vs. Re for various flows. The figure displays data of figure 5 (see its caption) for the symmetric (s)-flow regime. For $Re \gtrsim 10^4$ in the direction of rotation (-), the high-torque branch (stars) corresponds to the (b)-flow regime, i.e. to the “turbulent bifurcation”. Since both motors do not deliver the same torque in this \mathcal{R}_π -symmetry broken (b)-flow, the average of both values has been plotted. Some data for flat disks of standard machine shop roughness, operated in pure water up to 25Hz (squares and $Re^{-1/4}$ fit) are also displayed. Another $-1/4$ power law is fitted for the positive direction of rotation for $330 \leq Re \leq 1500$ and is displayed between $Re = 10^2$ and $Re = 10^4$.

inertial regime does not occur below a very high-Reynolds number owing to the very small roughness of the blades faces. This could be why both curves in figure 5 look so different: the lower one looks qualitatively like a low-roughness boundary flow and the upper one looks like a high-roughness boundary flow. Anyway, this may only account for a part of the flow driving: the resistive torque is much higher for any bladed impellers than for flat disks as shown in figure 13.

As a main result of its paper, Goldenfeld (2006) claims that full understanding of turbulence requires explicit accounting for boundary roughness: our observation of the closed von Kármán turbulent flow does not contradict this proposition at all.

5.4. High-Reynolds number: towards multistability and turbulent bifurcation

The von Kármán flow driven by high-curvature bladed impellers rotating in the negative direction presents another original behaviour: Ravelet *et al.* (2004) have shown that the turbulent von Kármán flow can exhibit multistability at high-Reynolds number. To study and analyze this phenomenon, it is necessary to introduce an additional parameter with respect to the present paper study: the rotation velocity difference $\Delta f = f_2 - f_1$ between the two impellers. The so-called “Turbulent bifurcation” and multistability are observed exclusively for the negative direction of rotation. So, the $\Delta f = 0$ regime presented along this paper —called (s) for symmetric in Ravelet *et al.* (2004)— can be observed only if both motors are started together, *i.e.*, if Δf is kept equal to zero at anytime. Once some velocity difference is applied long enough —depending of the magnitude of $|\Delta f|$ —, the flow changes abruptly to a one cell flow with axial pumping towards one of the impellers only instead of towards each impeller. This new flow —called (b) for bifurcated in Ravelet *et al.* (2004)— strongly breaks the \mathcal{R}_π -symmetry, has no middle shear-layer and requires much higher torque from the motors: typically 3 times the value of (s)-flow, with a finite difference between the two motors. The mean reduced torque at $\Delta f = 0$ is plotted with stars in figure 13: branches (s) and (b) co-exist for $Re \gtrsim 10^4$.

It is worth noting that this multistability can only be observed above Re_t , *i.e.* for flows with a well developed turbulent inertial Kolmogorov cascade. Furthermore, cycles in the parameter plane $\{Kp_2 - Kp_1; f_2 - f_1\}$ have been made for various Re between 100 and 3×10^5 (Ravelet 2005). At low-Reynolds numbers — $Re \lesssim 800$ —, this cycle is reduced to a continuous, monotonic and reversible line in the parameter plane. The first apparition of “topological” transformations of this simple line into multiples discontinuous branches of a more complex cycle is reported at $Re \simeq 5 \times 10^3$, in the neighborhood of the transitional Reynolds number Re_t , and multistability for $\Delta f = 0$ is first observed for $Re \sim 10^4$. The extensive study of this turbulent bifurcation with varying Re will be reported elsewhere.

From the above preliminary report of our results, we emphasize the fact that the turbulent bifurcation seems really specific of fully developed turbulent flows. Whereas the exact counter-rotating flow will not bifurcate (Ravelet *et al.* 2004), for $0 < |\Delta f|/f \ll 1$, this turbulent bifurcation around $Re = 10^4$ will correspond to a first order transition on the way to infinite Reynolds number dynamics. This flow really appears as an ideal prototype of an ideal system undergoing a succession of well-defined transitions on the way from order to high-Reynolds-number turbulence.

5.5. Conclusions

The von Kármán shear-flow with inertial stirring has been used for a global study of the transition from order to turbulence. The transition scenario is consistent with a globally supercritical scenario and this system appears as a very powerful table-top prototype for such type of study.

Many results of the present study proceed from velocity data collected in the middle of the shear-layer and we have shown that this layer and its chaotic/turbulent wandering can be responsible for the frequency content of the chaotic/turbulent spectrum of the data.

Further studies currently in progress invoke both a wider range of data in space, with the use of Particle Image Velocimetry, and a wider range in Reynolds number. Owing to the conclusions driven from the study of the azimuthal velocity variance, it is very appealing to characterize further the statistical properties of the turbulent velocity.

Also, with the slightly different point of view of controlling the disorder level, we have also shown that a thin annulus located in the mid-plane of the flow modifies the dynamics of the shear-layer (Ravelet *et al.* 2005). This property was recently used in

the Von Kármán Sodium (VKS) experiment held at Cadarache, France and devoted to the experimental study of dynamo action in a turbulent liquid sodium flow. Dynamo has effectively been observed for the first time in this system with a von Kármán configuration using, among other characteristics, an annulus in the mid-plane (Monchaux *et al.* 2006a). Moreover, clear evidence has been made that the mixing-layer large-scale patterns have a strong effect on the magnetic field induction at low frequency (Volk *et al.* 2006; Ravelet *et al.* 2006). Further studies of this effect in water experiments are under progress.

We are particularly indebted to Vincent Padilla and Cécile Gasquet for building up and piloting the experiment. We acknowledge Caroline Nore for making her simulations available, Arnaud Guet for his help on the visualisations and Frédéric Da Cruz for the viscosity measurements. We have benefited of very fruitful discussions with B. Dubrulle, N. Leprovost, L. Marié, R. Monchaux, C. Nore, J.-F. Pinton and R. Volk.

REFERENCES

- BATCHELOR, G. K. 1951 Note on a class of solutions of the navier-stokes equations representing steady rotationally-symmetric flow. *Quart. Journ. Mech. and Applied Math.* **4**, 29.
- BENZI, R. 2005 Flow reversal in a simple dynamical model of turbulence. *Phys. Rev. Letters* **95**, 024502.
- VAN DEN BERG, T. H., DOERING, C. R., LOHSE, D. & LATHROP, D. P. 2003 Smooth and rough boundaries in turbulent taylor-couette flow. *Phys. Rev. E* **68**, 036307.
- BERGE, P., POMEAU, Y. & VIDAL, C. 1984 *L'Ordre dans le Chaos*. Paris: Hermann, english translation: Wiley (1986).
- BOURGOIN, M., MARIÉ, L., PÉTRÉLIS, F., GASQUET, C., GUIGON, A., LUCIANI, J.-B., MOULIN, M., NAMER, F., BURGUETE, J., CHIFFAUDEL, A., DAVIAUD, F., FAUVE, S., ODIER, P. & PINTON, J.-F. 2002 Mhd measurements in the von Kármán sodium experiment. *Phys. Fluids* **14**, 3046.
- BUCHHAVE, P., GEORGE, W. K. & LUMLEY, J. L. 1979 The measurement of turbulence with the laser-doppler anemometer. *Ann. Rev. Fluid Mech.* **11**, 443.
- CADOT, O., COUDER, Y., DAERR, A., DOUADY, S. & TSINOBER, A. 1997 Energy injection in closed turbulent flows: Stirring through boundary layers versus inertial stirring. *Phys. Rev. E* **56**, 427.
- CADOT, O., DOUADY, S. & COUDER, Y. 1995 Characterization of the low-pressure filaments in a three-dimensional turbulent shear flow. *Phys. Fluids* **7**, 630.
- COCHRAN, W. G. 1934 The flow due to a rotating disk. *Proc. Cambridge Phil. Soc.* **30**, 365.
- COULLET, P. & IOOSS, G. 1990 Instabilities of one-dimensional cellular patterns. *Phys. Rev. Letters* **64**, 866.
- CRAWFORD, J.D. & KNOBLOCH, E. 1991 Symmetry and symmetry-breaking bifurcations in fluid dynamics. *Ann. Rev. Fluid Mech.* **23**, 341.
- CROSS, M.C. & HOHENBERG, P.C. 1993 Pattern formation outside of equilibrium. *RMP* **65**, 851.
- DAUCHOT, O. & MANNEVILLE, P. 1997 Local versus global concepts in hydrodynamic stability theory. *J. Phys. II France* **7**, 371.
- DOUADY, S., COUDER, Y. & BRACHET, M. E. 1991 Direct observation of the intermittency of intense vorticity filaments in turbulence. *Phys. Rev. Letters* **67**, 983.
- DUTTA, P. & HORN, P. M. 1981 Low-frequency fluctuations in solid: 1/f noise. *Rev. Mod. Physics* **53**, 497.
- ESCUDIER, M. P. 1984 Observations of the flow produced in a cylindrical container by a rotating endwall. *Experiments in Fluids* **2**, 189.
- FAUVE, S., LAROCHE, C. & CASTAING, B. 1993 Pressure fluctuations in swirling turbulent flows. *J. Phys. II France* **3**, 271.
- FRISCH, U. 1995 *Turbulence - The legacy of A. N. Kolmogorov*. New-York: Cambridge University Press.
- GAUTHIER, G., GONDRET, P. & RABAUD, M. 1999 Axisymmetric propagating vortices in the

- flow between a stationary and a rotating disk enclosed by a cylinder. *J. Fluid Mech.* **386**, 105.
- GELFGAT, A. Y., BAR-YOSEPH, P. Z. & SOLAN, A. 1996 Steady states and oscillatory instability of swirling flow in a cylinder with rotating top and bottom. *Phys. Fluids* **8**, 2614.
- GIOIA, G. & CHAKRABORTY, P. 2006 Turbulent friction in rough pipes and the energy spectrum of the phenomenological theory. *Phys. Rev. Letters* **96**, 044502.
- GOLDENFELD, N. 2006 Roughness-induced critical phenomena in a turbulent flow. *Phys. Rev. Letters* **96**, 044503.
- GROSSMANN, S. 2000 The onset of shear flow turbulence. *Rev. Mod. Physics* **72**, 603.
- HARRIOTT, G. M. & BROWN, R. A. 1984 Flow in a differentially rotated cylindrical drop at moderate Reynolds number. *J. Fluid Mech.* **144**, 403.
- HODGMAN, C. D., ed. 1947 *Handbook of chemistry and physics, thirtieth edition*. Chemical rubber publishing co.
- VON KÁRMÁN, T. 1921 Über laminäre und turbulente Reibung. *Z. Angew. Math. Mech.* **1**, 233.
- KOLMOGOROV, N. 1991a Dissipation of energy in the locally isotropic turbulence. *Proceedings of the Royal Society (London) Series A* **434**, 15, english traduction.
- KOLMOGOROV, N. 1991b The local structure of turbulence in incompressible viscous fluid for very large Reynolds number. *Proceedings of the Royal Society (London) Series A* **434**, 9, english traduction.
- LA PORTA, A., VOTH, G. A., CRAWFORD, A. M., ALEXANDER, J. & BODENSCHATZ, E. 2001 Fluid particle acceleration in fully developed turbulence. *Nature* **409**, 1017.
- LABBÉ, R., PINTON, J.-F. & FAUVE, S. 1996 Power fluctuations in turbulent swirling flows. *J. Phys II France* **6**, 1099.
- LATHROP, D. P., FINEBERG, J. & SWINNEY, H. L. 1992 Transition to shear-driven turbulence in couette-taylor flow. *Phys. Rev. A* **46**, 6390.
- LEPROVOST, N., MARIÉ, L. & DUBRULLE, B. 2004 A stochastic model of torque in von Kármán swirling flow. *Euro. Phys. Journal B* **39**, 121.
- LESIEUR, M. 1990 *Turbulence in Fluids*, second revised edition edn. Kluwer academic publishers.
- LUMLEY, J. L. 1965 Interpretation of time spectra measured in high-intensity shear flows. *Phys. Fluids* **8**, 1056–1062.
- MANNEVILLE, P. 1990 *Dissipative structures and weak turbulence*. Academic Press.
- MARIÉ, L. 2003 Transport de moment cinétique et de champ magnétique par un écoulement tourbillonnaire turbulent: influence de la rotation. PhD thesis, Université Paris VII.
- MARIÉ, L., BURGUETE, J., DAVIAUD, F. & LÉORAT, J. 2003 Numerical study of homogeneous dynamo based on experimental von Kármán type flows. *Euro. Phys. Journal B* **33**, 469.
- MARIÉ, L. & DAVIAUD, F. 2004 Experimental measurement of the scale-by-scale momentum transport budget in a turbulent shear flow. *Phys. Fluids* **16**, 457.
- MELLOR, G. L., CHAPPLE, P. J. & STOKES, V. K. 1968 On the flow between a rotating and a stationary disk. *J. Fluid Mech.* **31**, 95.
- MOISY, F., WILLAIME, H., ANDERSEN, J. S. & TABELING, P. 2001 Passive scalar intermittency in low temperature helium flows. *Phys. Rev. Letters* **86**, 4827.
- MONCHAUX, R., BERHANU, M., BOURGOIN, M., MOULIN, M., ODIER, PH., PINTON, J.-F., VOLK, R., FAUVE, S., MORDANT, N., PÉTRÉLIS, F., CHIFFAUDEL, A., DAVIAUD, F., DUBRULLE, B., GASQUET, C., MARIÉ, L. & RAVELET, F. 2006a Generation of magnetic field by dynamo action in a turbulent flow of liquid sodium. Submitted to *Phys. Rev. Letters*.
- MONCHAUX, R., RAVELET, F., DUBRULLE, B., CHIFFAUDEL, A. & DAVIAUD, F. 2006b Properties of steady states in turbulent axisymmetric flows. *Phys. Rev. Letters* **96**, 124502.
- NGUYEN, T. T., BIADILLAH, Y., MONGRAIN, R., BRUNETTE, J., TARDIF, J.-C. & BERTRAND, O. F. 2004 A method for matching the refractive index and kinematic viscosity of a blood analog for flow visualization in hydraulic cardiovascular models. *Journal of Biomechanical Engineering* **126** (4), 529–535.
- NIKURADSE, J. 1932 Gesetzmäßigkeiten der turbulenten stromungen in glatten rohren. *vDI Forschungsheft* **356**, in English, in NASA TT F-10 (1966), p. 359.
- NIKURADSE, J. 1933 Stromungsgesetz in rauhren rohren. *vDI Forschungsheft* **361**, in English, in Technical Memorandum 1292, National Advisory Committee for Aeronautics (1950).

- NORE, C., MOISY, F. & QUARTIER, L. 2005 Experimental observation of near-heteroclinic cycles in the von Kármán swirling flow. *Phys. Fluids* **17**, 064103.
- NORE, C., TARTAR, M., DAUBE, O. & TUCKERMAN, L. S. 2004 Survey of instability thresholds of flow between exactly counter-rotating disks. *J. Fluid Mech.* **511**, 45.
- NORE, C., TUCKERMAN, L. S., DAUBE, O. & XIN, S. 2003 The 1:2 mode interaction in exactly counter-rotating von Kármán swirling flow. *J. Fluid Mech.* **477**, 51.
- PINTON, J.-F. & LABBÉ, R. 1994 Correction to the Taylor hypothesis in swirling flows. *J. Phys. II France* **4**, 1461.
- RAVELET, F. 2005 Bifurcations globales hydrodynamiques et magnétohydrodynamiques dans un écoulement de von Kármán turbulent. PhD thesis, Ecole Polytechnique, France.
- RAVELET, F., CHIFFAUDEL, A., DAVIAUD, F. & LEORAT, J. 2005 Toward an experimental von Kármán dynamo: Numerical studies for an optimized design. *Phys. Fluids* **17**, 117104.
- RAVELET, F., MARIÉ, L., CHIFFAUDEL, A. & DAVIAUD, F. 2004 Multistability and memory effect in a highly turbulent flow: Experimental evidence for a global bifurcation. *Phys. Rev. Letters* **93**, 164501.
- RAVELET, F., VOLK, R., BEHRANU, M., CHIFFAUDEL, A., DAVIAUD, F., DUBRULLE, B., FAUVE, S., MONCHAUX, R., MORDANT, N., ODIER, PH., PÉTRÉLIS, F. & PINTON, J.-F. 2006 Magnetic induction in a turbulent flow of liquid sodium: mean behaviour and slow fluctuations. Submitted to *J. Fluid Mech.*
- SCHLICHTING, H. 1979 *Boundary-Layer Theory*, 7th edn. McGraw-Hill.
- SCHOUVEILER, L., GAL, P. LE & CHAUVE, M.-P. 2001 Instabilities of the flow between a rotating and a stationary disk. *J. Fluid Mech.* **443**, 329.
- SØRENSEN, J. B. & CHRISTENSEN, E. A. 1995 Direct numerical simulation of rotating fluid flow in a closed cylinder. *Phys. Fluids* **7**, 764.
- SPOHN, A., MORY, M. & HOPFINGER, E. J. 1998 Experiments on vortex breakdown in a confined flow generated by a rotating disc. *J. Fluid Mech.* **370**, 73.
- STEWARTSON, K. 1953 On the flow between two rotating coaxial disks. *Proc. Cambridge Philos. Soc.* **49**, 333.
- TABELING, P., ZOCCHI, G., BELIN, F., MAURER, J. & WILLAIME, H. 1996 Probability density functions, skewness and flatness in large Reynolds number turbulence. *Phys. Rev. E* **53**, 1613.
- TENNEKES, H. & LUMLEY, J. L. 1972 *A first course in turbulence*. MIT Press.
- TITON, J.-H. & CADOT, O. 2003 The statistics of power injected in a closed turbulent flow: Constant torque forcing versus constant velocity forcing. *Phys. Fluids* **15**, 625.
- VOLK, R., ODIER, P. & PINTON, J.-F. 2006 Fluctuation of magnetic induction in von Kármán swirling flows. *Phys. Fluids* **18**, 085105.
- ZANDBERGEN, P. J. & DIJKSTRA, D. 1987 von Kármán swirling flows. *Ann. Rev. Fluid Mech.* **19**, 465.
- ZOCCHI, G., TABELING, P., MAURER, J. & WILLAIME, H. 1994 Measurement of the scaling of the dissipation at high Reynolds numbers. *Phys. Rev. E* **50**, 3693.